GHz Broadband SH0 Mode Lithium Niobate Acoustic Delay Lines

Ruochen Lu, *Member, IEEE*, Yansong Yang, *Member, IEEE*, Ming-Huang Li, *Member, IEEE*, Tomás Manzaneque, *Member, IEEE*, and Songbin Gong, *Senior Member, IEEE*

***Abstract*— We present the first group of GHz broadband SH0 mode acoustic delay lines (ADLs). The implemented ADLs adopt unidirectional transducer designs in a suspended X-cut lithium niobate thin film. The design space of the SH0 mode ADLs at GHz is first theoretically investigated, showing that the large coupling and sufficient spectral clearance to adjacent modes collectively enable the broadband performance of SH0 delay lines. The fabricated devices show 3-dB fractional bandwidth ranging from 4% to 34.3% insertion loss between 3.4 and 11.3 dB. Multiple delay lines have been demonstrated with center frequencies from 0.7 to 1.2 GHz, showing great frequency scalability. The propagation characteristics of SH0 in lithium niobate thin film are experimentally extracted. The demonstrated ADLs can potentially facilitate broadband signal processing applications.**

***Index Terms*— Acoustic delay lines (ADLs), enhanced mobile broadband (eMBB), lithium niobate, microelectromechanical systems, piezoelectricity, SH0 modes.**

I. Introduction

THE emerging enhanced mobile broadband (eMBB) applications for fifth-generation (5G) communication are calling for unprecedented signal processing capabilities [1], [2]. Targeting at a thousand-fold increase in the mobile data volume per unit area [3], novel broadband signal processing functions at radio frequency (RF) are highly sought-after. Acoustic devices, in which RF signals are converted into and processed in the acoustic domain before the conversion back to the electromagnetic (EM) domain, are great candidates for providing such low-loss wideband signal processing capabilities for their three key advantages. First, acoustic devices are miniature because of their significantly shorter wavelength (λ) compared to the EM counterparts [4], therefore suitable for handheld and mobile applications. Second, various signal processing functions can be passively implemented by designing the transfer function of the transducers and waveguides [5]. Thus, acoustic devices do not compete with the power-hungry analog-to-digital converters (ADCs) and digital signal processors (DSPs) in the follow-on stages for the power budget [6]. Third, the recent development of high electromechanical coupling (k^2) piezoelectric platforms [7]–[13] has demonstrated record-low loss over a wide bandwidth (BW), thus overcoming the high insertion loss (IL) and narrow BW bottleneck that have been precluding acoustic signal processing from eMBB applications.

Among different acoustic devices at RF, acoustic delay lines (ADLs) have been demonstrated for a wide range of applications, including transversal filters [14], [15], correlators [16], time-domain equalizers [17], oscillators [18], sensors [19], amplifiers [20], [21], and time-varying nonreciprocal systems [22]. These diverse signal processing functions can all be implemented by tailoring the transducers [23] and waveguides [24]. Conventionally, ADLs are built based on surface acoustic wave (SAW) platforms [25]–[27]. However, their performance, namely the substantial IL and the narrow fractional bandwidth (FBW), is fundamentally curbed by the moderate k^2 and achievable reflectivity of the transducers [28], [29], even in designs targeting low loss such as single-phase unidirectional transducers (SPUDTs) [30]. Recently, ADLs based on lateral modes in lithium niobate ($LiNbO_3$) thin films have been demonstrated with fundamental shear horizontal (SH0) mode [23], [31] or fundamental symmetrical (S0) mode [32]–[34], showing significantly improved IL-FBW design space. The enhanced performance is collectively enabled by large k^2 (up to 40%) [35]–[37], the notable reflectivity in the embedded reflectors [31], [34], and the low propagation loss (PL) in single crystal quality ($LiNbO_3$) thin films [32], [34].

However, it remains challenging to achieve broadband performance with the current demonstrations for two reasons. First, although large FBW has been obtained [23], [31]–[33], the absolute BW of the demonstrations are limited because of their low center frequencies below 500 MHz. Second, the FBW of the high-frequency S0 mode demonstrations is also limited [34] by their adjacent modes that can cause the overlap of passbands. Therefore, to achieve broadband ADLs, it is paramount to first identify the suitable acoustic mode with large k^2, low loss, sufficient spectral clearance to adjacent modes, and scalability to the GHz frequency range. Among various candidates, the SH0 mode in X-cut $LiNbO_3$ is promising. SH0 ADLs have been experimentally demonstrated with high k^2 and low loss at lower frequencies [31]. Moreover, high-frequency SH0 mode acoustic devices have been reported with a sparse mode space [38]–[41]. However, due to the

Manuscript received May 12, 2019; accepted September 19, 2019. Date of publication September 24, 2019; date of current version January 24, 2020. This work was supported in part by the Defense Advanced Research Projects Agency (DARPA) Microsystems Technology Office (MTO) Near Zero Power RF and Sensor Operations (N-ZERO) Program and in part by the DARPA MTO Signal Processing at RF (SPAR) Program. *(Corresponding author: Ruochen Lu.)*

The authors are with the Department of Electrical and Computing Engineering, University of Illinois at Urbana–Champaign, Urbana, IL 61801 USA (e-mail: rlu10@illinois.edu).

Digital Object Identifier 10.1109/TUFFC.2019.2943355

highly dispersive characteristics of the mechanical modes in thin-film $LiNbO_3$ [42], it is nontrivial to scale up the operating frequency. To advance $LiNbO_3$ ADLs for broadband applications at 700 MHz or beyond [43], [44], this work aims to demonstrate the first GHz-range, broadband ADLs based on the SH0 mode in $LiNbO_3$.

In this work, the design space of GHz broadband SH0 mode ADLs is first discussed. The implemented ADLs show 3-dB FBW ranging from 4% to 34.3% and IL between 3.4 and 11.3 dB. Multiple ADLs have been demonstrated with center frequencies from 0.7 to 1.2 GHz. The PL of SH0 at 1.08 GHz is extracted as 0.0182 dB per wavelength (dB/λ), and the phase velocity is 4255 m/s. The demonstrated ADLs can potentially facilitate broadband applications at the GHz range.

This article is organized as follows. Section II provides a general discussion on the design of the SH0 mode ADLs. The ADL topology is first introduced and followed with an analysis of the characteristics of SH0 at the GHz range. The theoretical performance limitations will be presented. Then, the dispersion curves of different modes in X-cut $LiNbO_3$ will be presented, determining the large achievable BW of the GHz SH0 ADLs. Section III presents the fabricated GHz ADLs. Section IV discusses the measurement results of the devices with different delay lengths, center frequencies, and BW. The SH0 wave propagation characteristics, including the PL and phase velocities, are experimentally derived. Finally, the conclusion is stated in Section V.

II. Design of SH0 Broadband Acoustic Delay Lines

A. Unidirectional Acoustic Delay Line Overview

The schematic of a typical SH0 mode ADL is shown in Fig. 1. The ADL consists of 135-nm aluminum interdigitated transducers on top of a suspended 800-nm $LiNbO_3$ thin film. A pair of free boundaries exist in the transverse direction for defining the acoustic waveguide. A pair of SPUDT transducers are placed on the opposite ends of the ADL. The SPUDTs are composed of cascaded transducer unit cells, and each cell includes a pair of transduction electrodes (λ/8 wide) and one grounded distributed acoustic reflector (3λ/8 wide) [14], [28], [29]. The transduction center is in the center of one of the transduction electrodes because the gap between two grounded electrodes causes no transduction [28]. The reflection center is in the center of the reflector because the pair of λ/8 electrodes causes no reflection based on the multireflection theory [28]. In each cell, the transduction center is placed nonsymmetrically from the reflectors on both sides. The nonsymmetry causes a difference in the phase delays of the waves reflected from the reflectors on the opposite sides. As a result, the reflected wave propagating toward the forward direction (FWD) constructively interferes with the wave launched toward FWD, while the reflected wave propagating toward the backward direction (BWD) destructively interferes with the wave launched toward BWD [28], [34]. Therefore, with a sufficient amount of cascaded reflectors, a significant cancellation of the BWD wave propagation can be achieved, resulting in the removal of the bidirectionality in the transducers and an IL reduction for the ADL.

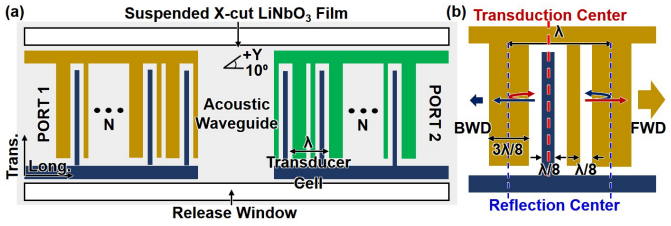

Fig. 1. (a) Mockup of an SH0 mode ADL with a pair of SPUDT transducers on a suspended X-cut $LiNbO_3$ thin film. The transverse and longitudinal directions are labeled. (b) Layout of an SPUDT unit cell.

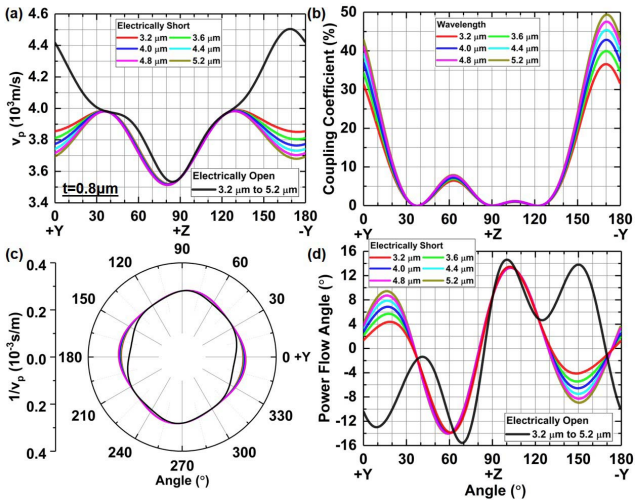

Fig. 2. Simulated characteristics of SH0 at different in-plane orientations in a 0.8-μm-thick X-cut $LiNbO_3$ thin film. (a) Phase velocity with electrically open and short boundary conditions. (b) k^2. (c) Slowness curve. (d) PFA of SH0 at different longitudinal wavelengths.

The GHz SH0 ADLs are oriented at $-10°$ to the $+$Y-axis in X-cut $LiNbO_3$ for two reasons. First, the SH0 mode at such an orientation features a large k^2, while the other modes (e.g., S0 and A0) have much smaller k^2 ($<$5%) [42]. The dependence of k^2 on the in-plane orientation can be analyzed via finite-element analysis (FEA) in COMSOL [see Fig. 2(a)], starting from the phase velocities of SH0 under electrically open and short boundary conditions. The phase velocity in a $LiNbO_3$ film with the electrically short boundary condition (v_m) is smaller than that with the electrically open boundary condition (v_f), which is caused by the piezoelectric softening effect [42]. The dispersion of SH0 near 1 GHz is also plotted in Fig. 2(a). SH0 at a larger λ has a slower phase velocity in an electrically shorted $LiNbO_3$ film (3684–3853 m/s), while SH0 in an electrically open film is barely dispersive (4504 m/s). k^2 is then calculated with the obtained phase velocities [45], [46]. The maximum k^2 is obtained at $-10°$ to the $+$Y-axis [see Fig. 2(b)]. Consistent with the dispersion of v_p, lower frequency SH0 (larger λ) has slightly larger k^2 (40% at 1 GHz).

The second reason for the selected orientation is to attain a small power flow angle (PFA) for SH0 so that longer delay ADLs can be attained [47]. The PFA is defined as the angle between the phase velocity and the group velocity (pointing to the phase velocity). PFAs for acoustic waves in anisotropic materials (e.g., $LiNbO_3$) are not always zero [48].

If the PFA is significant, the acoustic waves launched in our delay structure would bounce between free boundaries in the transverse direction (see Fig. 1). For ADLs with longer delays, the acoustic energy might leak out from the bus line area (without SPUDTs for collecting the energy). Detailed discussions on performance degradation of longer ADLs from significant PFAs have been discussed in [34]. The PFA is derived from the slope of the slowness curve of GHz SH0 waves [see Fig. 2(c)] and presented in Fig. 2(d). It can be observed that the PFAs of SH0 in the film with electrically open and short conditions have different signs near the orientation with the highest k^2. The PFA of SH0 in a $LiNbO_3$ film with the electrically open condition reaches zero at $-11°$ to the +Y-axis, while PFA for that with electrically short condition reaches zero at $-6°$ to the +Y-axis. The dispersion phenomena can also be observed with similar crossover points. To sum up, due to the large k^2 and small PFA, GHz SH0 ADLs are placed oriented at $-10°$ to the +Y-axis in X-cut $LiNbO_3$.

B. Broadband SH0 Acoustic Delay Lines at GHz

Based on the structure introduced in Section II-A, the performance limitations of GHz SH0 ADLs are evaluated. As stated in the introduction, both the performance limitations of the SH0 ADL and the frequency spacing of SH0 to the adjacent modes at GHz are critical for broadband applications. This section will investigate both aspects.

Two performance bounds, namely the piezoelectric limitation and the reflectivity limitation, define the performance of SPUDT-based ADL [28]. The piezoelectric limitation sets the maximum 3-dB FBW that a device can achieve without trading off IL [28]. The maximum FBW is directly related to k^2 of the intended mode and the effective coupling efficiency of the transducer in the chosen platform. The limitation can be presented as [28], [49]

$$\text{IL} = \text{FBW}^2 \cdot Q_T / c_{\text{piezo}}, \quad \text{when FBW} > \sqrt{c_{\text{piezo}}/Q_T} \tag{1}$$

$$c_{\text{piezo}} = \frac{v_f - v_m}{v_f} \cdot \left[1 + \frac{3(v_f - v_m)}{2v_f}\right] \tag{2}$$

where Q_T is the normalized quality factor of the transducer and is determined by the transduction structure. c_{piezo} is the material piezoelectric constant determined by the material coupling coefficient. Especially, for the SPUDT configuration, Q_T is 0.659 [28]. For our design where λ is 3.6 μm, v_f is 4502 m/s, and v_m is 3807 m/s [see Fig. 2(a)], the coupling coefficient is 40%. From (2), c_{piezo} is 0.190. Therefore, we can plot the piezoelectric limit of GHz SH0 ADLs on the IL-FBW trade space with the forbidden region marked in gray [see Fig. 3(a)]. It shows a significantly enlarged design space (up to 65%) when compared with the conventional piezoelectric platforms with lower k^2 (<10%). Note that the performance bounds vary among devices with different λ values, because c_{piezo}, as a function of k^2, is slightly dispersive [see Fig. 2(b)]. For instance, over the wavelength range of interest, c_{piezo} is 0.175 when λ is 3.2 μm, while c_{piezo} is 0.231 when λ is 5.2 μm. Such dispersion leads to smaller forbidden regions for ADLs with larger λ.

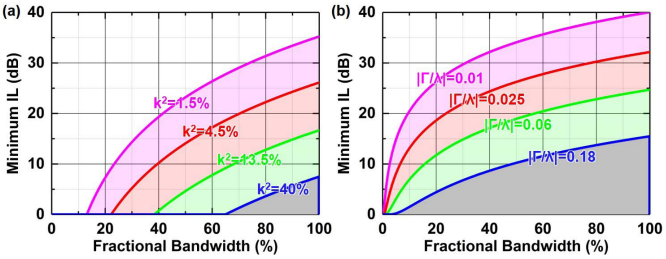

Fig. 3. Performance tradeoff between minimum IL and FBW of SPUDT in various platforms with (a) different coupling coefficients and (b) different reflectivities per wavelength. The design space below each curve is the forbidden region for a given platform with such characteristics. The gray regions are plotted for SH0 SPUDTs with λ of 3.6 μm on 800-nm $LiNbO_3$.

The second performance limitation is caused by the finite attainable unidirectionality provided by the embedded reflectors. To achieve a certain IL, more reflectors (thus more cells) are needed for a platform with less reflectivity per cell. An increased number of cells lead to narrower BW of the transfer functions (FBW $\sim$ 1/N). Such a performance bound can be expressed as [28]

$$\text{IL} = 1 - e^{-\Gamma_\lambda/\text{FBW}} \tag{3}$$

where Γ_λ is the reflection per wavelength and can be calculated based on the mechanically induced reflection (Γ_m) and electrically induced reflection (Γ_e) as [31]

$$\Gamma_\lambda = \frac{\Gamma_m + \Gamma_e}{1 + \Gamma_m \cdot \Gamma_e} \tag{4}$$

$$\Gamma_m = \Gamma_{\text{su}} e^{j\alpha} \frac{1 - e^{-j2\alpha}\left(1 - \Gamma_{\text{su}}^2\right)}{1 - \Gamma_{\text{su}}^2 e^{-j2\alpha}} \tag{5}$$

$$\Gamma_e = \Gamma_{0\infty} e^{j\alpha} \frac{1 - e^{-j2\alpha}\left(1 - \Gamma_{0\infty}^2\right)}{1 - \Gamma_{0\infty}^2 e^{-j2\alpha}} \tag{6}$$

where Γ_{su} and $\Gamma_{0\infty}$ are the step-up mechanical and electrical reflection coefficients in the interface between the metallized and unmetallized sections, respectively. α is the electrical width of the reflector, which is $3\pi/4$ for our SPUDT. Γ_{su} can be extracted from the COMSOL FEA simulation using the mechanical scattering parameter approach explained in [24] and [31]. For our specific design with 135-nm Al on 800-nm $LiNbO_3$, Γ_{su} is -0.047. Thus, Γ_m can be calculated as -0.066j. The imaginary part refers to a $-90°$ phase difference for the reflected wave. $\Gamma_{0\infty}$ can be extracted from v_m and v_f [31]. For v_f of 4502 m/s and v_m of 3807 m/s [see Fig. 2(a)], $\Gamma_{0\infty}$ is -0.084. Thus, Γ_e is calculated to be -0.118j. Using (4), Γ_λ is -0.183j. Such Γ_λ is considerably larger than that of the incumbent SAW technology (-0.06j), collectively resulted from the larger Γ_m due to the larger k^2 and the larger Γ_m from the suspended thin-film structure. The design space is shown on the IL-FBW tradeoff figure with the forbidden region marked in gray [see Fig. 3(b)]. It can be seen that for GHz SH0 mode ADLs, the achievable reflectivity is currently the limiting factor, and the minimum IL for ADLs with FBW of 4%, 8%, 16%, and 32% is 0.1, 0.9, 3.2, and 7.2 dB, respectively, which have surpassed the theoretical limits of the state-of-the-art (SOA) of SAW ADLs [28]. It is noteworthy that these performance limits are first-order

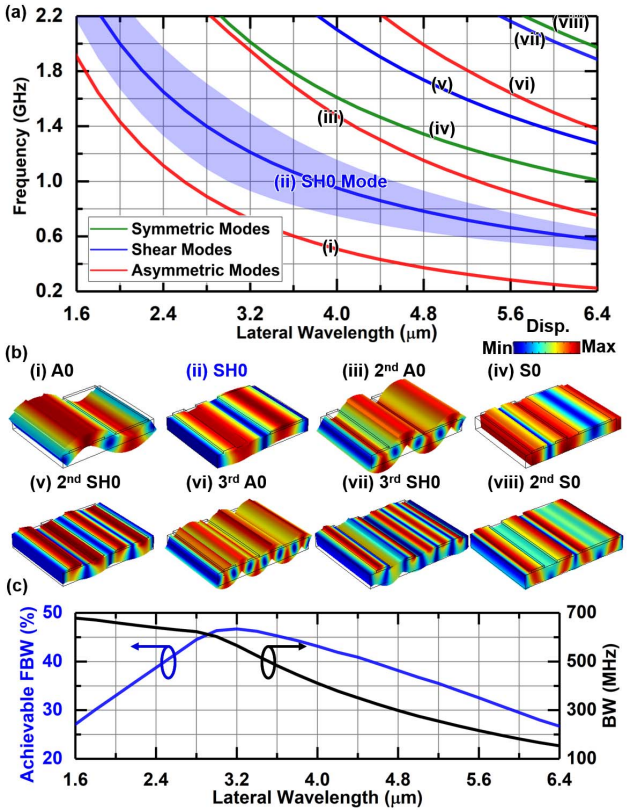

Fig. 4. (a) Dispersion curves of different modes in an 800-nm-thick X-cut $LiNbO_3$ thin film sorted into symmetrical, shear, and asymmetric modes. The achievable BW is highlighted in the figure. (b) Displacement mode shapes of different modes as labeled in the dispersion curve. (c) Extracted achievable FBW and BW with different λ values.

estimations based on the continuity approximation [28], [29], and more accurate IL-FBW tradeoff will be presented in Section II-C using the FEA.

The second key factor for enabling broadband ADLs is the spectral spacing between the mode of interest and the adjacent modes. If the passbands of the primary mode and the spurious modes partially overlap, ADL performance degradation occurs for two causes. First, over the overlapped frequency range, the spurious modes distort the transmission and reflection because part of the energy is coupled into the undesired mode, introducing ripples in the scattering parameters. Second, the spurious modes cause notable ripples in the group delay due to the fact that different modes have different phase velocities and thus produce various group delays.

The FEA is used to identify the dispersion curves of various modes in a single SPUDT cell with λ between 1.6 and 6.4 μm (SH0 frequency 0.6–2 GHz). Periodic boundary conditions are applied to the lateral edges. The dispersion curves of asymmetric modes, shear modes, and symmetric modes are plotted in Fig. 4(a) with their displacement mode shapes presented in Fig. 4(b). Due to the dispersion of the modes in thin-film $LiNbO_3$, the spectral spacing between the SH0 and the first-order A0 modes sets the maximum FBW at shorter wavelengths, while the spectral spacing between the SH0 and second-order A0 modes sets the maximum FBW at longer wavelengths. Note that the term second order refers to that two longitudinal wavelengths exist within a cell (i.e., with a transverse mode order of 2), while the zero in "A0" refers to the number of displacement nulls in the thickness direction. The maximum achievable FBW can be quantitatively calculated based on the admittance transfer function of a pair of IDTs with the cell number $N(>1)$, approximated as [50]

$$|H(\omega)| = \omega h_0 e^{-j\beta L} \cdot \sin^2(N_t \beta W_p/2)/\sin^2(\beta W_p/2) \quad (7)$$

where ω is the angular frequency, h_0 is a coupling constant related to the material properties and acoustic wave mode, L is the distance between the center of the transducers, N_t is the number of transducer pairs, W_p is the cell length, and β is the wave vector $(2\pi/\lambda)$. Such an admittance transfer function follows the sinc-squared function, and the BW is inversely proportional to N and independent of the k^2 of the mode. That is, for an ADL with a specific topology, different modes would have the same BW. Based on the above analysis, the maximum achievable FBW of GHz SH0 ADLs can be approximated as

$$\mathrm{FBW}_{\max} = 2 \cdot \min\left(\frac{f_{\mathrm{SH0}} - f_{\mathrm{A0}}}{f_{\mathrm{SH0}} + f_{\mathrm{A0}}}, \frac{f_{\mathrm{2nd\_A0}} - f_{\mathrm{SH0}}}{f_{\mathrm{SH0}} + f_{\mathrm{2nd\_A0}}}\right) \quad (8)$$

where f_{SH0}, f_{A0}, and $f_{\mathrm{2nd\_A0}}$ are the frequencies of the SH0, the A0, and the second-order A0 modes, respectively. The calculated FBW is plotted in Fig. 4(c), reaching a maximum of 46.7% at $\lambda = 3.2$ μm. The FBW is above 30% for devices between 0.6 and 2 GHz, demonstrating a vast design space across different frequencies [as highlighted in Fig. 4(a)]. The absolute BW is also presented in Fig. 4(c), showing its increase toward the GHz frequency range and saturation near 1.2 GHz due to the decrease in FBW. The center frequency where the FBW maximizes is determined by the film thickness [34]. Wider FBW and BW can be expected for higher frequency SH0 ADLs built on thinner $LiNbO_3$ films. For our first demonstration of broadband GHz SH0 ADLs, 800-nm $LiNbO_3$ is selected based on the in-house fabrication capabilities.

C. Simulation and Design of Key Parameters

After theoretically investigating the design space of broadband SH0 ADLs in $LiNbO_3$, a COMSOL FEA is used to capture the intricacies and understand the frequency-domain responses. As presented in [34], 2-D simulations are set up with periodic boundary conditions applied to the transverse edges of the ADL for both the mechanical and electrical domains [24]. Perfectly matched layers are applied to the longitudinal ends of the ADL. The simulation assumes lossless conditions in both the electrical and mechanical domains because the loss factors are currently not well understood and remain an active area of experimental research [34], [52].

In the simulation, the film stack is set as 135-nm aluminum electrodes on an 800-nm single-crystal X-cut $LiNbO_3$ [34]. λ is set as 3.6 μm and the gap length (L_g) is 0.4 mm, while the cell number (N) varies from 3 to 20. Fig. 5(a) shows the displacement mode shape of the ADL at the center frequency, demonstrating minimum power flow toward the BWD and thus validating the unidirectionality of SPUDT. Fig. 5(b) and (c) shows the simulated IL and RL with the ports conjugately matched. The IL-FBW tradeoff can be clearly

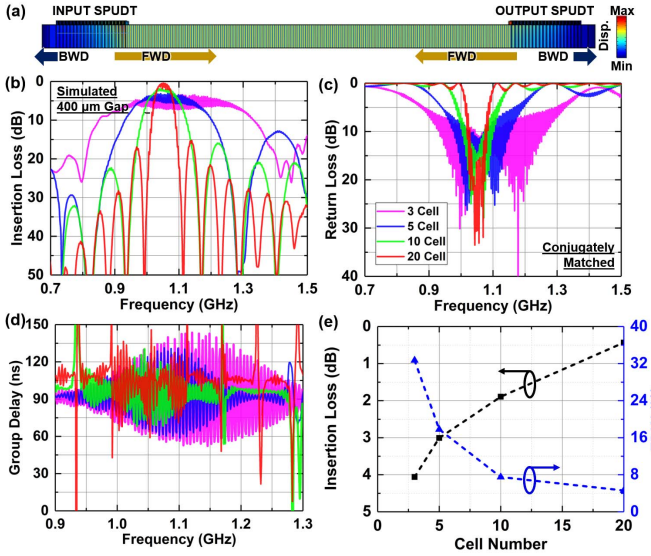

Fig. 5. Simulated performance of the GHz SH0 ADLs with a 3.6-μm cell length and the same gap length of 0.4 mm, but different numbers of SPUDT cells (3, 5, 10, and 20). (a) Cross-sectional mode shape depicting the unidirectionality of the SPUDT transducers for an ADL with 20 cells and a gap length of 0.4 mm. The thickness of the cross section is exaggerated. (b) IL. (c) RL. (d) Group delay. (e) Extracted IL and FBW, illustrating their tradeoff.

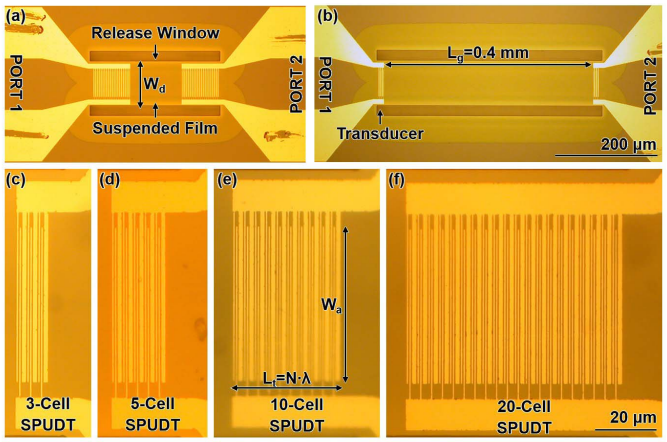

Symbol	Parameter	Value	Symbol	Parameter	Value
λ	Cell length (μm)	3.2-5.2	W_a	Aperture width (μm)	50
N	Number of cells	3-20	W_d	Device width (μm)	86
L_g	Gap length (mm)	0.1-1.6	L_T	Transducer length (μm)	10.8-104
T_{LN}	LiNbO3 thickness (nm)	800	T_{Al}	Aluminum thickness (nm)	135

Fig. 6. Optical microscope images of the fabricated SH0 mode ADLs. Zoomed-out images of ADLs with (a) 20-cell SPUDT with λ of 3.6 μm and L_g of 0.1 mm (Group A), and (b) three-cell SPUDT with λ of 3.6 μm and L_g of 0.4 mm (Group E). (c)–(f) Zoomed-in images of the SPUDT with N between 3 and 20 cells with λ of 3.6 μm (Group E). The key parameters are shown in the inset table.

observed and is summarized in Fig. 5(e). For the three-cell ADL, the IL is 4 dB, and the 3-dB FBW is 32.7%, while for the 20-cell ADL, the IL is 0.4 dB, and the 3-dB FBW is 4.6%. These results show a significantly improved IL-FBW design space in comparison to SOA. Fig. 5(d) shows the group delays around 100 ns for the miniature ADLs shorter than 0.6 mm. The ripples in the passband are caused by a combination of the internal reflections in the SPUDT [14] and the lack of adequate unidirectionality in the SPUDT with fewer cell numbers [34]. The group delay flatness can be further improved by weighting the transduction centers and reflection centers within a transducer [14] and also by increasing the reflectivity per reflector [32].

To sum up, we have explored the design space for GHz broadband SH0 ADLs in this section. The SPUDT ADL design is first presented based on the analysis on k^2, velocity, and PFA of SH0 at GHz. The maximum achievable FBW is then presented based on both the IL-FBW tradeoff of SPUDT designs (coupling and reflectivity limitations) and the analysis of the mode space. Finally, FEA is used to investigate the design intricacies and to obtain the frequency response.

III. Implementation of Acoustic Delay Lines

The devices were in-house fabricated with the process presented in [34]. ADLs are released with isotropic XeF_2 etching. An 800-nm X-cut $LiNbO_3$ thin film on a 4-in Si wafer is provided by NGK Insulators, Ltd., for the fabrication. The optical images of the fabricated ADLs are shown in Fig. 6. The devices show no visible warping under a microscope [see Fig. 6(a) and (b)] and the SPUDT transducers are well defined with high fidelity [see Fig. 6(c) and (d)]. The key design parameters, namely the cell length (λ), the gap length (L_g), and the number of cells (N), are labeled, and their typical values are presented in the inset table.

Six groups of SH0 ADLs are designed for a thorough understanding of the broadband performance space (see Table I). ADLs in Group A have the same transducer design (λ and N) but different L_g values for identifying the propagation parameters of SH0 at GHz. The device with L_g of 0.1 mm in Group A is also used for showing the power handling and nonlinearity. Group B includes ADLs with the same N of 20 and L_g of 0.1 mm, but different λ values, for exploring the frequency scalability and also validating the dispersion presented in Fig. 4. The minimum λ is limited to 3.2 μm due to the in-house lithography capability. Groups C and D are similar to Group B, but with different N values of 10 and 5, respectively, demonstrating the dependence of IL and FBW on N. A set of devices with a maximum FBW of 34.3% and a group delay of 100 ns is presented in Group E. Finally, the performance of all implemented SH0 ADLs (Group F) is summarized and compared. Devices in Group F have different λ between 3.2 and 5.2 μm, L_g between 0.1 and 1.6 mm, and N between 3 and 20. The extracted IL and FBW are compared with the performance bounds derived in Section II-B. Measured results and discussions will be presented in Section IV.

IV. Measurements and Discussion

A. Acoustic Delay Lines With Different Delays

The fabricated ADLs were first measured with a Keysight N5249A PNA-X network analyzer at the −10-dBm power level in air and then conjugately matched using the Keysight Advanced Design System. The conjugate match is crucial for maintaining the unidirectionality in SPUDTs [28]. ADLs in Group A ($N = 20$, $\lambda = 3.6$ μm, and $L_g = 0.1$–1.6 mm) are designed for investigating the propagation characteristics of

TABLE I
KEY PARAMETERS OF THE FABRICATED DEVICES

Index	Cell Length (μm)	Gap Length (mm)	No. of Cells	Meas. Fig.	Comments
Group A	3.6	0.1 – 1.6	20	7, 14	Gap Length & Nonlinearity
Group B	3.2 – 5.2	0.1	20	8-9	Cell No. & Wavelength
Group C	3.2 – 5.2	0.1	10	10	Cell No. & Wavelength
Group D	3.2 – 5.2	0.1	5	11	Cell No. & Wavelength
Group E	3.6	0.4	3-20	12-13	Broadband ADL
Group F	3.2 – 5.2	0.1 – 1.6	3-20	15	Performance Summary

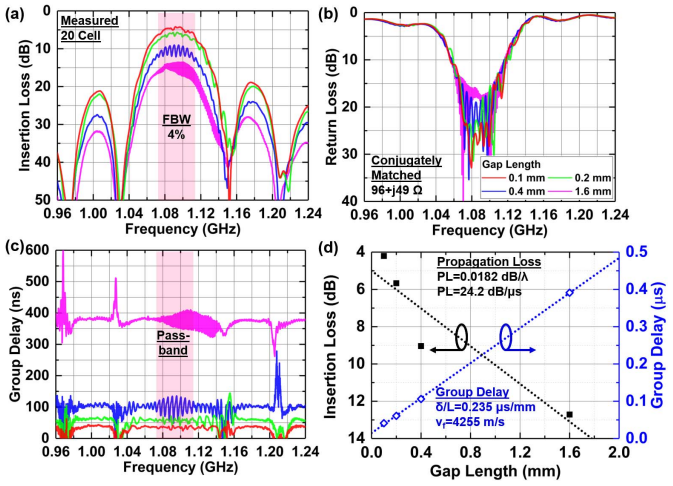

Fig. 7. Measured S-parameters of the SH0 ADLs (Group A, $N = 20$ and $\lambda = 3.6$ μm) with identical transducers but different L_g values (0.1–1.6 mm). (a) IL, (b) RL, and (c) group delay responses. (d) Extracted PL (24.2 dB/μs) and phase velocity (4255 m/s) of the SH0 mode in 800-nm X-cut $LiNbO_3$ at 1.1 GHz.

SH0 at GHz and demonstrating longer delays. The measured IL and RL are shown in Fig. 7(a) and (b) with the ports conjugately matched. The ADLs show a passband centered at 1.09 GHz. A minimum IL of 4.2 dB and a 3-dB FBW of 4% have been achieved for the ADL with a 0.1-mm gap length. An increase in the IL is observed for longer ADLs, which is collectively caused by the PL of SH0 in the $LiNbO_3$ waveguide and the additional power loss due to a slight PFA caused by the angular misalignment [34]. Group delays between 42 and 391 ns have been obtained [see Fig. 7(c)]. The in-band ripples in IL and group delays are collectively caused by the finite reflectivity in the embedded reflectors [28], the weakly resonant nature of SPUDT [14], and the nonzero PFA due to the angular misalignment in the implementation [34]. Further optimizations in the transducer designs and fabrication processes can mitigate the issue.

The propagation characteristics are experimentally extracted [see Fig. 7(d)], showing a PL of 24.2 dB/μs and a velocity of 4255 m/s for the SH0 mode in 800-nm X-cut $LiNbO_3$ at 1.1 GHz. The PL is higher than that of S0 mode at the same frequency [34], which agrees with the comparison in PL between S0 and SH0 at lower frequencies [23]. The velocity of SH0 is slower than that of S0 [34], leading to a shorter ADL for the same desired delay, but at the cost of achieving

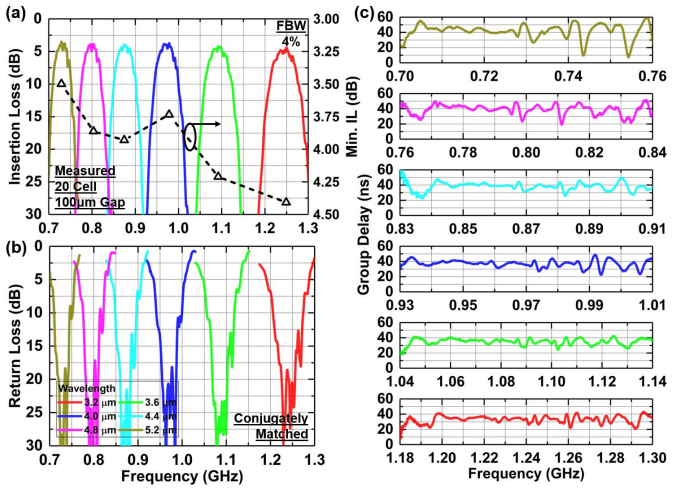

Fig. 8. Measured performance of the ADLs (Group B, $N = 20$ and $L_g = 0.1$ mm) with different λ values (3.2–5.2 μm) or center frequencies. (a) IL. (b) RL. (c) Measured group delays of different ADLs in their passbands.

lower center frequencies with the same feature size. Note that the current PL is exacerbated by the existing nonzero PFA. For example, the increased IL for the device with 0.4-mm L_g is likely caused by the nonzero PFA [34], leading to additional energy loss no less than 1.9 dB. The effects can be mitigated in future work using a wider aperture or slanted electrodes [53].

B. Acoustic Delay Lines With Different Center Frequencies

ADLs in Group B ($N = 20$, $L_g = 0.1$ mm, and $\lambda = 3.2$–5.2 μm) are designed for investigating the frequency scalability and also validate the dispersion curves (see Fig. 8). The fabricated 20-cell devices show clear passbands ranging from 0.7 to 1.2 GHz with a 3-dB FBW of 4%. An IL of 3.5 dB is achieved for the 0.7-GHz device, while an IL of 4.4 dB is attained for the 1.2-GHz device. The increasing IL at higher frequencies is likely caused by an increasing loss in both the electrical domain (larger series resistance in the IDTs and dielectric loss in $LiNbO_3$ thin film) [54] and the mechanical domain (larger PL) [52]. Delays around 40 ns have been obtained with the in-band ripples caused by finite directionality and the internal reflections of SPUDT [14].

The wideband performance of the SH0 ADLs is presented in Fig. 9. The highly dispersive nature of different modes in the thin-film $LiNbO_3$ can be observed, since the first-order A0 mode is closer to the SH0 mode for shorter λ and the second-order A0 mode is closer to the SH0 mode for longer λ. A clean spectrum without spurious modes in the adjacent spectrum can be observed, consequently enabling ADLs with larger FBWs.

C. Acoustic Delay Lines With Different Fractional Bandwidths

ADLs in Group C ($N = 10$, $L_g = 0.1$ mm, and $\lambda = 3.2$–5.2 μm) and Group D ($N = 5$, $L_g = 0.1$ mm, and $\lambda = 3.2$–5.2 μm) are designed for investigating the impact

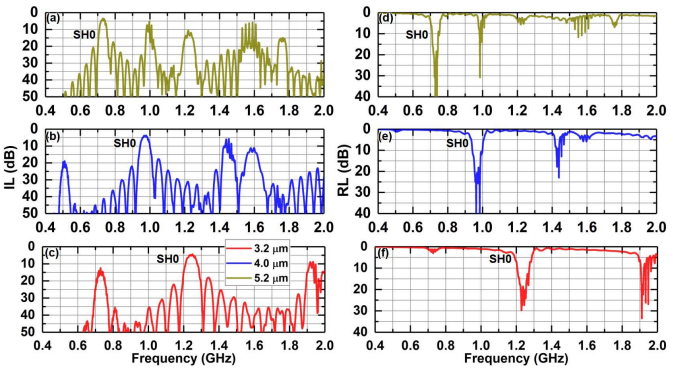

Fig. 9. Measured wideband performance of different devices in Group B. (a)–(c) IL. (d)–(f) RL. The adjacent modes exist as predicted in Fig. 4.

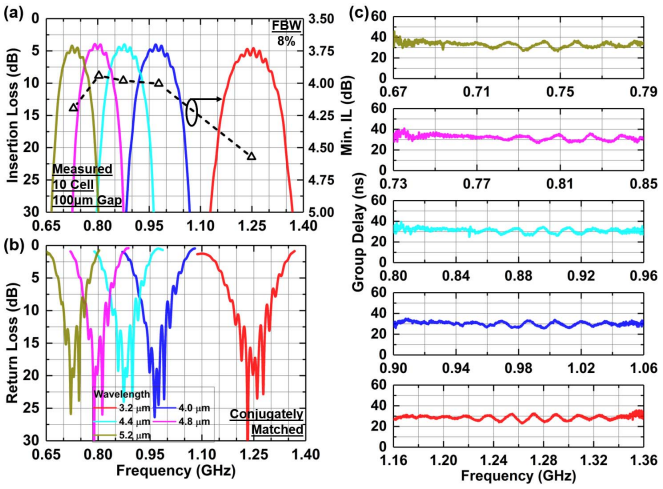

Fig. 10. Measured performance of the ADLs (Group C, $N = 10$ and $Lg = 0.1$ mm) with different λ values (3.2–5.2 μm) or center frequencies. (a) IL. (b) RL. (c) Measured group delays of different ADLs in their passbands.

of cell numbers on the FBW, when compared with ADLs in Group B (presented in Section IV-B, Fig. 8). The fabricated ten-cell devices (Group C, Fig. 10) have a 3-dB FBW of 8%, a minimum IL of 5.1 dB at 0.7 GHz, and a maximum IL of 5.6 dB at 1.1 GHz with group delays around 30 ns. The fabricated five-cell devices (Group D, Fig. 11) have a 3-dB FBW of 18%, a minimum IL of 4.8 dB at 0.7 GHz, and a maximum IL of 5.5 dB at 1.2 GHz with group delays around 25 ns.

When comparing ADLs in Groups B, C, and D, four differences can be observed. First, IL of ADLs with more cells is smaller, which is due to more energy propagating toward the FWD caused by more reflectors. Second, the FBW of ADLs with more cells is smaller, which is a direct result of a narrower band transfer function [see (7)]. These two results agree with the IL-FBW tradeoff. Third, group delays are longer for devices with more cells because of longer transducers in those devices. Finally, ADLs with fewer cells have larger ripples in the IL and group delay, because the triple travel signal (TTS) [28] is not effectively suppressed due to a lack of directionality in the SPUDT. These results demonstrate the large design space of GHz SH0 ADLs for various applications with different specifications.

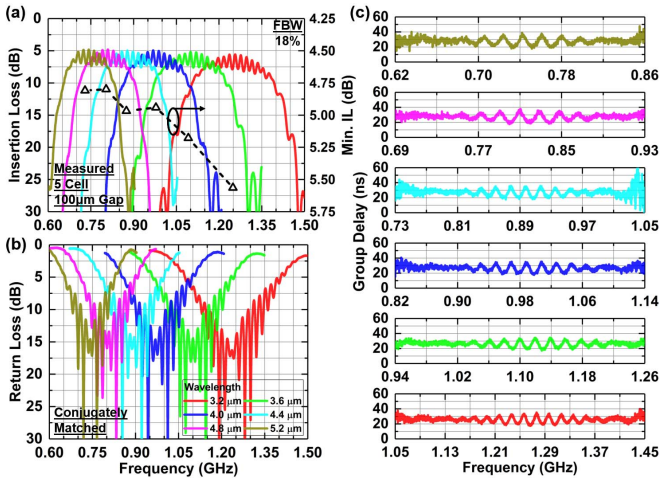

Fig. 11. Measured performance of the ADLs (Group C, $N = 5$ and $Lg = 0.1$ mm) with different λ values (3.2–5.2 μm) or center frequencies. (a) IL. (b) RL. (c) Measured group delays of different ADLs in their passbands.

TABLE II
IL BREAKDOWN OF ADLS IN GROUP E

Damping Source	3 Cell	5 Cell	10 Cell	20 Cell
Finite Uni-directionality	4.0 dB	3.0 dB	1.9 dB	0.4 dB
PL in Waveguide	2.0 dB	2.1 dB	2.2 dB	2.4 dB
IL due to Non-zero PFA	1.9 dB	1.9 dB	1.9 dB	1.9 dB
Others (e.g., Electrical Loading)	3.4 dB	3.9 dB	3.6 dB	4.3 dB
Total	11.3 dB	10.9 dB	9.6 dB	9.0 dB

D. Toward Broadband Acoustic Delay Lines

Due to the existence of PL, the TTS experiences three times larger PL when compared to the main signal. Therefore, for devices with larger PL from longer delays, the in-band ripples in IL and group delay are still relatively small for devices with even broader FBW (fewer cells). ADLs in Group E ($L_g = 0.4$ mm, $\lambda = 3.6$ μm, and $N = 3$–20) are designed for investigating the performance of ADLs with even broader FBW when a significant delay exists.

The measured IL and RL are presented in Fig. 12(a) and (b) with ports conjugately matched. For the device with 20 cells, an IL of 9.0 dB and a 3-dB FBW of 3.9% are obtained, while for the device with three cells, an IL of 11.3 dB and an FBW of 34.3% are shown. The extracted IL-FBW tradeoff is presented in Fig. 12(d), showing the same trend as that simulated in Fig. 5. The group delay is presented in Fig. 12(c), showing that the wider band ADLs do not have significantly increased ripples in the passbands due to PL. The IL breakdown is presented in Table II. It can be observed that the finite directionality is not the key loss contributor at GHz. The other main contributors are the PL, additional IL due to nonzero PFA, and other loss, including electrical loading from the resistance of IDTs and the dielectric loss in $LiNbO_3$. More studies on the loss mechanisms of acoustic waves in thin-film waveguides will be performed in the future.

The wideband performance is presented in Fig. 13, showing a clean spectrum without spurious modes in the passband, even for the device with 34.3% FBW. The current device is close

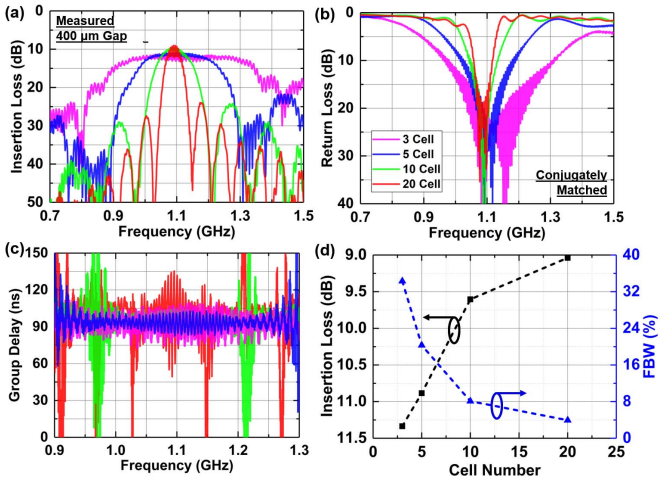

Fig. 12. Measured performance of the ADLs (Group E, $\lambda = 3.6$ μm and $L_g = 0.4$ mm) with different N values (3–20) or FBW. (a) IL. (b) RL. (c) Measured group delays of different ADLs in their passbands. (d) Extracted IL and FBW illustrating their tradeoff.

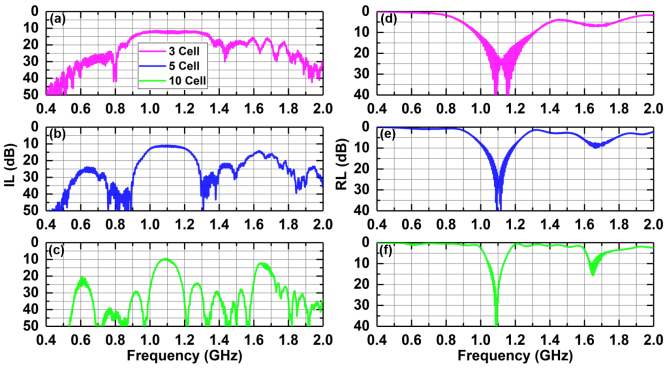

Fig. 13. Measured wideband performance of different devices in Group E. (a)–(c) IL. (d)–(f) RL. The large FBW has been achieved due to large spectral spacings between the SH0 and adjacent modes.

to the calculated maximum achievable FBW at this frequency (45%, Fig. 4). The demonstrated broadband ADLs are enabled due to the enhanced IL-FBW design space of the SH0 mode and the clean spectrum collectively. It is also feasible to further mitigate the spurious modes by the tracker changer designs using multistrip couplers [51].

E. Power Handling and Nonlinearity

The power handling capability of our system has been studied using the 100-μm gap length device in Group A [see Fig. 6(a)]. The device was measured in air at different power levels between −10 and 10 dBm [Fig. 14 (a)–(d)]. The device shows good linearity up to 5-dBm input power. At 10-dBm power level, the passband shifts to lower frequencies, and degradation of IL is observed. The frequency drift and performance degradation are likely caused by the thermal nonlinearity in $LiNbO_3$ devices, which causes a temperature rise at high power levels [55]. To further enhance the power handling capabilities in future implementations, additional anchors with embedded phononic crystal structures [24] could be leveraged

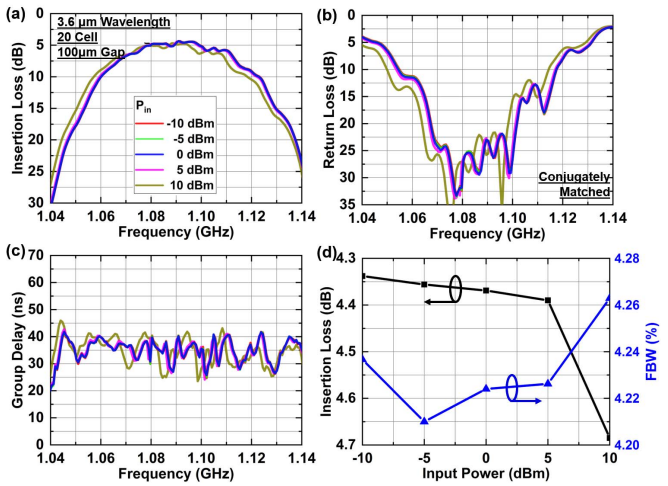

Fig. 14. Measured (a) IL, (b) RL, and (c) Group delay of the 100-μm gap length device in Group A at −10, −5, 0, 5, and 10 dBm. (d) Summarized IL and FBW at different power levels.

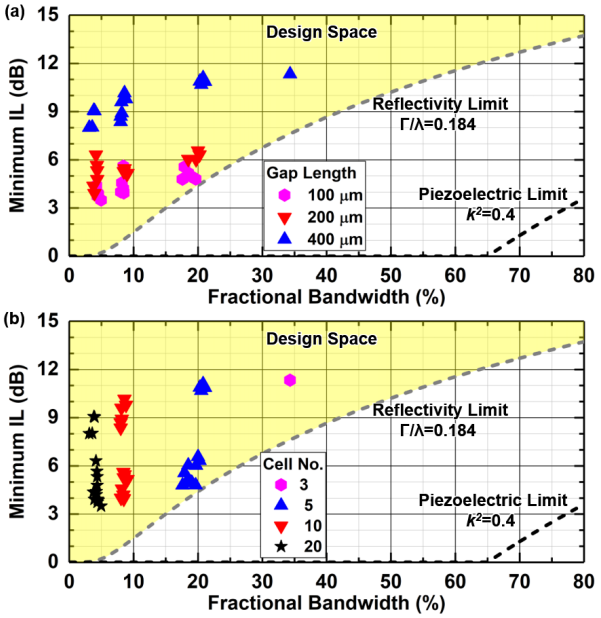

Fig. 15. Design space validation for GHz SH0 ADLs. The demonstrated devices are labeled and sorted based on (a) gap length and (b) cell number, respectively.

to enlarge the thermal conductance while maintaining the acoustic confinement. Detailed modeling and approaches to mitigate the nonlinearity will be studied in future work.

F. Performance Summary

To comprehensively study the design space of broadband SH0 ADLs at GHz, IL, and FBW of all implemented SH0 ADLs (Group F) are extracted and plotted on the IL-FBW tradeoff space (see Fig. 15). Devices in Group F have different λ between 3.2 and 5.2 μm, L_g between 0.1 and 1.6 mm, and N between 3 and 20. The data points are first sorted based on the gap length in Fig. 15(a), showing that the propagation-related losses (PL and additional IL from nonzero

PFA) are the main source of the IL. The impact of cell number on the performance is then presented in Fig. 15(b), showing that different specifications can be met for various applications using different designs. The demonstrated performance surpasses the SAW SOA and opens up new design space for eMBB applications.

V. Conclusion

In this work, we have demonstrated GHz broadband SH0 ADLs in lithium niobate. The design space of GHz SH0 ADLs has been fully investigated based on both the IL-FBW tradeoff and the spectral spacing between the SH0 and adjacent modes, showing that the large k^2, large reflectivity from the thin film structure, and the clean spectrum near SH0 mode collectively enable the broadband performance. The implemented ADLs show 3-dB FBWs ranging from 4% to 34.3% and IL between 3.4 and 11.3 dB over the frequency range from 0.7 to 1.2 GHz. The PL and phase velocity of SH0 at 1.08 GHz are extracted as 0.0182 dB/λ and 4255 m/s, respectively. Power handling and nonlinearity have also been measured. The demonstrated SH0 delay platform could potentially provide broadband passive signal processing capabilities for future eMBB applications.

VI. Acknowledgment

The authors would like to thank Dr. T. Olsson for helpful discussions.

References

[1] P. Popovski, K. F. Trillingsgaard, O. Simeone, and G. Durisi, "5G wireless network slicing for eMBB, URLLC, and mMTC: A communication-theoretic view," *IEEE Access*, vol. 6, pp. 55765–55779, 2018.

[2] A. Anand, G. De Veciana, and S. Shakkottai, "Joint scheduling of URLLC and eMBB traffic in 5G wireless networks," in *Proc. IEEE INFOCOM IEEE Conf. Comput. Commun.*, Apr. 2018, pp. 1970–1978.

[3] E. Hossain, M. Rasti, H. Tabassum, and A. Abdelnasser, "Evolution toward 5G multi-tier cellular wireless networks: An interference management perspective," *IEEE Wireless Commun.*, vol. 21, no. 3, pp. 118–127, Jun. 2014.

[4] R. Ruby, "A snapshot in time: The future in filters for cell phones," *IEEE Microw. Mag.*, vol. 16, no. 7, pp. 46–59, Aug. 2015.

[5] R. H. Tancrell and M. G. Holland, "Acoustic surface wave filters," *Proc. IEEE*, vol. 59, no. 3, pp. 393–409, Mar. 1971.

[6] M. T.-C. Lee, V. Tiwari, S. Malik, and M. Fujita, "Power analysis and minimization techniques for embedded DSP software," *IEEE Trans. Very Large Scale Integr. (VLSI) Syst.*, vol. 5, no. 1, pp. 123–135, Mar. 1997.

[7] L. Colombo, A. Kochhar, C. Xu, G. Piazza, S. Mishin, and Y. Oshmyansky, "Investigation of 20% scandium-doped aluminum nitride films for MEMS laterally vibrating resonators," in *Proc. IEEE Int. Ultrason. Symp. (IUS)*, Sep. 2017, pp. 1–4.

[8] L. Colombo, A. Kochhar, G. Vidal-Álvarez, and G. Piazza, "X-cut lithium niobate laterally vibrating MEMS resonator with figure of merit of 1560," *J. Microelectromech. Syst.*, vol. 27, no. 4, pp. 602–604, Aug. 2018.

[9] C. Cassella, Y. Hui, Z. Qian, G. Hummel, and M. Rinaldi, "Aluminum Nitride Cross-Sectional Lamé Mode Resonators," *J. Microelectromech. Syst.*, vol. 25, no. 2, pp. 275–285, Apr. 2016.

[10] R. R. Benoit, R. Q. Rudy, J. S. Pulskamp, R. G. Polcawich, and S. S. Bedair, "Advances in piezoelectric PZT-based RF MEMS components and systems," *J. Micromech. Microeng.*, vol. 27, no. 8, Jul. 2017, Art. no. 083002.

[11] Y. Yang, R. Lu, L. Gao, and S. Gong, "4.5 GHz lithium niobate MEMS filters with 10% fractional bandwidth for 5G front-ends," *J. Microelectromech. Syst.*, vol. 28, no. 4, pp. 575–577, Aug. 2019.

[12] M. Park, Z. Hao, D. G. Kim, A. Clark, R. Dargis, and A. Ansari, "A 10 GHz single-crystalline scandium-doped aluminum nitride lamb-wave resonator," in *Proc. 20th Int. Conf. Solid-State Sens., Actuators Microsyst Eurosensors XXXIII (TRANSDUCERS EUROSENSORS XXXIII)*, Jun. 2019, pp. 450–453.

[13] M. Kadota, T. Ogami, K. Yamamoto, H. Tochishita, and Y. Negoro, "High-frequency Lamb wave device composed of MEMS structure using $LiNbO_3$thin film and air gap," *IEEE Trans. Ultrason., Ferroelectr., Freq. Control*, vol. 57, no. 11, pp. 2564–2571, Nov. 2010.

[14] J. M. Hode, J. Desbois, P. Difilie, M. Solal, and P. Ventura, "SPUDT-based filters: Design principles and optimization," in *Proc. IEEE Int. Ultrason. Symp. Int. Symp.*, vol. 1, Nov. 1995, pp. 39–50.

[15] G. Martin, F. Z. Bi, D. P. Chen, and C. S. Lam, "Synthesizing and optimizing SPUDT SAW filters," in *Proc. IEEE Int. Ultrason. Symp.*, vol. 1, Oct. 1998, pp. 165–168.

[16] T. Manzaneque, R. Lu, Y. Yang, and S. Gong, "An SH0 lithium niobate correlator for orthogonal frequency coded spread spectrum communications," in *Proc. IEEE Int. Freq. Control Symp.*, Jul. 2017, pp. 143–147.

[17] R. Lu, T. Manzaneque, Y. Yang, M.-H. Li, and S. Gong, "Towards digitally addressable delay synthesis: GHz low-loss acoustic delay elements from 20 ns to 900 ns," in *Proc. IEEE Int. Conf. Micro Electro Mech. Syst.*, Jan. 2019.

[18] D. Ciplys *et al.*, "GaN-based SAW delay-line oscillator," *Electron. Lett.*, vol. 37, no. 8, pp. 545–546, Apr. 2001.

[19] J. Devkota, P. R. Ohodnicki, and D. W. Greve, "SAW sensors for chemical vapors and gases," *Sensors*, vol. 17, no. 4, p. 801, 2017.

[20] S. Ghosh, "FDSOI on lithium niobate using Al2O3 wafer-bonding for acoustoelectric RF microdevices," in *Proc. 20th Int. Conf. Solid-State Sens., Actuators Microsyst. Eurosensors XXXIII (TRANSDUCERS EUROSENSORS XXXIII)*, Jun. 2019, pp. 535–538.

[21] L. Hackett *et al.*, "High-gain leaky surface acoustic wave amplifier in epitaxial InGaAs on lithium niobate heterostructure," *Appl. Phys. Lett.*, vol. 114, no. 25, Jun. 2019, Art. no. 253503.

[22] R. Lu, T. Manzaneque, Y. Yang, L. Gao, A. Gao, and S. Gong, "A radio frequency nonreciprocal network based on switched acoustic delay lines," *IEEE Trans. Microw. Theory Techn.*, vol. 67, no. 4, pp. 1516–1530, Apr. 2019.

[23] T. Manzaneque, R. Lu, Y. Yang, and S. Gong, "Lithium niobate MEMS chirp compressors for near zero power wake-up radios," *J. Microelectromech. Syst.*, vol. 26, no. 6, pp. 1204–1215, Dec. 2017.

[24] R. Lu, T. Manzaneque, Y. Yang, and S. Gong, "Lithium niobate phononic crystals for tailoring performance of RF laterally vibrating devices," *IEEE Trans. Ultrason., Ferroelectr., Freq. Control*, vol. 65, no. 6, pp. 934–944, Jun. 2018.

[25] S. Lehtonen, V. P. Plessky, C. S. Hartmann, and M. M. Salomaa, "SPUDT filters for the 2.45 GHz ISM band," *IEEE Trans. Ultrason., Ferroelectr., Freq. Control*, vol. 51, no. 12, pp. 1697–1703, Dec. 2004.

[26] C. L. Grasse and D. A. Gandolfo, "Acoustic surface wave dispersive delay lines as high resolution frequency discriminator," in *Proc. IEEE Int. Ultrason. Symp*, Oct. 1972, pp. 233–236.

[27] W. R. Shreve and R. L. Baer, "Reduced insertion-loss broadband SAW delay lines," in *Proc. IEEE Int. Ultrason. Symp*, Oct. 1987, pp. 155–160.

[28] C. S. Hartmann and B. P. Abbott, "Overview of design challenges for single phase unidirectional SAW filters," in *Proc. IEEE Int. Ultrason. Symp*, Oct. 1989, pp. 79–89.

[29] T. Kodama, H. Kawabata, H. Sato, and Y. Yasuhara, "Design of low–loss saw filters employing distributed acoustic reflection transducers," *Electron. Commun. Jpn., Electron.*, vol. 70, no. 9, pp. 32–44, 1987.

[30] C. S. Hartmann, P. V. Wright, R. J. Kansy, and E. M. Garber, "An analysis of SAW interdigital transducers with internal reflections and the application to the design of single-phase unidirectional transducers," in *Proc. IEEE Int. Ultrason. Symp*, Oct. 1982, pp. 40–45.

[31] T. Manzaneque, R. Lu, Y. Yang, and S. Gong, "Low-loss and wideband acoustic delay lines," *IEEE Trans. Microw. Theory Techn.*, vol. 67, no. 4, pp. 1379–1391, Apr. 2019.

[32] R. Lu, T. Manzaneque, Y. Yang, and S. Gong, "S0-mode lithium niobate acoustic delay lines with 1 dB insertion loss," in *Proc. IEEE Int. Ultrason. Symp.*, Oct. 2018, pp. 1–9.

[33] G. Vidal-Álvarez, A. Kochhar, and G. Piazza, "Delay lines based on a suspended thin film of X-cut lithium niobate," in *Proc. IEEE Int. Ultrason. Symp.*, Sep. 2017, pp. 1–4.

[34] R. Lu, T. Manzaneque, Y. Yang, M.-H. Li, and S. Gong, "Gigahertz low-loss and wideband S0 mode lithium niobate acoustic delay lines," *IEEE Trans. Ultrason., Ferroelectr., Freq. Control*, vol. 66, no. 8, pp. 1373–1386, Aug. 2019.
[35] S. Gong and G. Piazza, "Design and analysis of lithium–niobate-based high electromechanical coupling RF-MEMS resonators for wideband filtering," *IEEE Trans. Microw. Theory Techn.*, vol. 61, no. 1, pp. 403–414, Jan. 2013.
[36] R. H. Olsson, III, *et al.*, "A high electromechanical coupling coefficient SH0 Lamb wave lithium niobate micromechanical resonator and a method for fabrication," *Sens. Actuators A, Phys.*, vol. 209, pp. 183–190, Mar. 2014.
[37] R. Wang, S. A. Bhave, and K. Bhattacharjee, "Design and fabrication of S_0Lamb-wave thin-film lithium niobate micromechanical resonators," *J. Microelectromech. Syst.*, vol. 24, no. 2, pp. 300–308, Apr. 2015.
[38] R. Lu, T. Manzaneque, Y. Yang, J. Zhou, H. Hassanieh, and S. Gong, "RF filters with periodic passbands for sparse Fourier transform-based spectrum sensing," *J. Microelectromech. Syst.*, vol. 27, no. 5, pp. 931–944, Oct. 2018.
[39] M. Kadota, Y. Ishii, and S. Tanaka, "Ultra-wideband T- and p-type ladder filters using a fundamental shear horizontal mode plate wave in a $LiNbO_3$ plate," *Jpn. J. Appl. Phys.*, vol. 58, no. SG, Jun. 2019, Art. no. SGGC10.
[40] M. Kadota, Y. Kuratani, T. Kimura, M. Esashi, and S. Tanaka, "Ultra-wideband and high frequency resonators using shear horizontal type plate wave in $LiNbO(_3)$ thin plate," *Jpn. J. Appl. Phys.*, vol. 53, no. 7S, Jun. 2014, Art. no. 07KD03.
[41] M. Kadota, T. Ogami, T. Kimura, and K. Daimon, "Tunable filters using wideband elastic resonators," *IEEE Trans. Ultrason., Ferroelectr., Freq. Control*, vol. 60, no. 10, pp. 2129–2136, Oct. 2013.
[42] I. E. Kuznetsova, B. D. Zaitsev, S. G. Joshi, and I. A. Borodina, "Investigation of acoustic waves in thin plates of lithium niobate and lithium tantalate," *IEEE Trans. Ultrason., Ferroelectr., Freq. Control*, vol. 48, no. 1, pp. 322–328, Jan. 2001.
[43] *Decision (EU) 2017/899 of the European Parliament and of the Council of 17,May 2017 on the use of the 470-790 MHz frequency band in the Union*, document OJ L 138, 25.5.2017, 2017.
[44] J. Lee, E. Tejedor, K. Ranta-Aho, H. Wang, K.-T. Lee, E. Semaan, E. Mohyeldin, J. Song, C. Bergljung, and S. Jung, "Spectrum for 5G: Global status, challenges, and enabling technologies," *IEEE Commun. Mag.*, vol. 56, no. 3, pp. 12–18, Mar. 2018.
[45] *Federal Standards Committee of the IEEE Ultrasonics and Frequency Control Society*, Standard 176-1987-IEEE Standard on Piezoelectricity, 1987.
[46] R. Lu, M.-H. Li, Y. Yang, T. Manzaneque, and S. Gong, "Accurate extraction of large electromechanical coupling in piezoelectric MEMS resonators," *J. Microelectromech. Syst.*, vol. 28, no. 2, pp. 209–218, Apr. 2019.
[47] I. E. Kuznetsova, B. D. Zaitsev, A. A. Teplykh, S. G. Joshi, and A. S. Kuznetsova, "The power flow angle of acoustic waves in thin piezoelectric plates," *IEEE Trans. Ultrason., Ferroelectr., Freq. Control*, vol. 55, no. 9, pp. 1984–1991, Sep. 2008.
[48] R. S. Weis and T. K. Gaylord, "Lithium niobate: Summary of physical properties and crystal structure," *Appl. Phys. A, Solids Surf.*, vol. 37, no. 4, pp. 191–203, Aug. 1985.
[49] C. S. Hartmann, S. Jen, M. A. Domalewski, and J. C. Andle, "Improved accuracy for determining SAW transducer capacitance and K^2," in *Proc. IEEE Int. Ultrason. Symp*, Oct. 1987, pp. 161–168.
[50] K. Hashimoto, *Surface Acoustic Wave Devices in Telecommunications: Modelling and Simulation*. Berlin, Germany: Springer, 2013.
[51] F. G. Marshall, C. O. Newton, and E. G. S. Paige, "Theory and design of the surface acoustic wave multistrip coupler," *IEEE Trans. Microw. Theory Techn.*, vol. MTT-21, no. 4, pp. 206–215, Apr. 1973.
[52] I. L. Bajak, A. McNab, J. Richter, and C. D. W. Wilkinson, "Attenuation of acoustic waves in lithium niobate," *J. Acoust. Soc. Amer.*, vol. 69, no. 3, pp. 689–695, Mar. 1981.
[53] M. Goto, H. Yatsuda, and T. Chiba, "Power flow angles for slanted finger surface acoustic wave filters on langasite substrate," *Jpn. J. Appl. Phys.*, vol. 46, no. 7, p. 4744, 2007.
[54] R. T. Schermer and T. H. Stievater, "Millimeter-wave dielectric properties of highly refractive single crystals characterized by waveguide cavity resonance," *IEEE Trans. Microw. Theory Techn.*, vol. 67, no. 3, pp. 1078–1087, Mar. 2019.
[55] R. Lu and S. Gong, "Study of thermal nonlinearity in lithium niobate-based MEMS resonators," in *Proc. 18th Int. Solid-State Sens., Actuators Microsyst. Conf. (TRANSDUCERS)*, Jun. 2015, pp. 8–11.

Ruochen Lu (S'14–M'19) received the B.E. degree (Hons.) in microelectronics from Tsinghua University, Beijing, China, in 2014, and the M.S. and Ph.D. degrees in electrical engineering from the University of Illinois at Urbana–Champaign (UIUC), Urbana, IL, USA, in 2017 and 2019, respectively.

He is currently a Postdoctoral Researcher with UIUC. His research interests include radio frequency microsystems and their applications for timing and signal processing.

Dr. Lu was a recipient of the Best Student Article Awards at the 2017 IEEE International Frequency Control Symposium and the 2018 IEEE International Ultrasonics Symposium, the 2015 Lam Graduate Award from the College of Engineering, UIUC, the 2017 Nick Holonyak, Jr. Graduate Research Award, the 2018 Nick Holonyak, Jr. Fellowship, and the 2019 Raj Mittra Outstanding Research Award from the Department of Electrical and Computer Engineering, UIUC.

Yansong Yang (S'15–M'19) received the B.S. degree in electrical and electronic engineering from the Huazhong University of Science and Technology, Wuhan, China, in 2014, and the M.S. and Ph.D. degrees in electrical engineering from the University of Illinois at Urbana–Champaign, Urbana, IL, USA, in 2017 and 2019, respectively.

He is currently a Postdoctoral Researcher with UIUC. His research interests include design and microfabrication techniques of MEMS resonators, filters, and switches for RF front ends and wake-up systems.

Dr. Yang has won Second Place in the Best Article Competition at the 2018 International Microwave Symposium and has been a finalist for the Best Article Award at the 2018 IEEE International Frequency Control Symposium. He was also a recipient of the 2019 P. D. Coleman Graduate Research Award from the Department of Electrical and Computer Engineering, UIUC.

Ming-Huang Li (S'11–M'15) received the B.S. degree in mechanical engineering (minor in electrical engineering) from National Chung Cheng University, Chiayi, Taiwan, in 2009, and the M.S. and Ph.D. degrees from the Institute of NanoEngineering and MicroSystems, National Tsing Hua University (NTHU), Hsinchu, Taiwan, in 2011 and 2015, respectively.

He is currently an Assistant Professor with the Department of Power Mechanical Engineering, NTHU. Prior to joining NTHU, he was with the Micro and Nanotechnology Laboratory, University of Illinois at Urbana–Champaign, Urbana, IL, USA, as a Postdoctoral Researcher. His research interests include micromechanical resonator and oscillator design for wireless communication and signal processing, MEMS-ASIC integration technologies, and interface circuit design for MEMS-based microsystems.

Dr. Li was a recipient of the Outstanding Engineering Student Scholarship from the Chinese Institute of Engineers in 2009, the CTCI Foundation Science and Technology Research Scholarship in 2014, and the Young Scholar Fellowship from the Ministry of Science and Technology, Taiwan, in 2019. He has won the Best Student Article Award at the 2011 Joint Conference of the IEEE International Frequency Control Symposium and the European Frequency and Time Forum (IFCS-EFTF 2011).

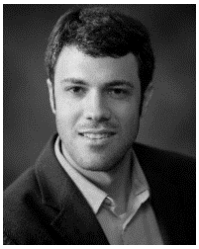

Tomás Manzaneque (M'14) received the Ph.D. degree in industrial engineering from the University of Castilla–La Mancha, Ciudad Real, Spain, in 2015, focusing on applying piezoelectric MEMS resonators as sensors for measuring the density and viscosity of liquids.

In 2015, he joined the Micro and Nanotechnology Laboratory, University of Illinois at Urbana–Champaign, Urbana, IL, USA, as a Postdoctoral Researcher. During this period, he focused on acoustic devices for low-power radio receivers in the Internet of Things applications. In 2018, he moved to the Delft University of Technology, Delft, The Netherlands, as a Postdoctoral Researcher, where he is currently working on microfluidic MEMS for biological applications. He has authored or coauthored over 20 journal articles covering the design, modeling, characterization, and integration of piezoelectric microdevices.

Songbin Gong (S'06–A'09–M'12–SM'17) received the Ph.D. degree in electrical engineering from the University of Virginia, Charlottesville, VA, USA, in 2010.

He is currently an Associate Professor and an Intel Alumni Fellow with the Department of Electrical and Computer Engineering and the Micro and Nanotechnology Laboratory, University of Illinois at Urbana–Champaign, Urbana, IL, USA. His research primarily focuses on design and implementation of radio frequency microsystems, components, and subsystems for reconfigurable RF front ends. In addition, his research explores hybrid microsystems based on the integration of MEMS devices with photonics or circuits for signal processing and sensing.

Dr. Gong is a Technical Committee Member of MTT-21 RF-MEMS of the IEEE Microwave Theory and Techniques Society, the International Frequency Control Symposium, and the International Electron Devices Meeting. He was a recipient of the 2014 Defense Advanced Research Projects Agency Young Faculty Award, the 2017 NASA Early Career Faculty Award, and the 2019 UIUC College of Engineer Dean's Award for Excellence in Research. Along with his students and postdocs, he received the Best Article Awards from the 2017 and 2019 IEEE International Frequency Control Symposium, the 2018 International Ultrasonics Symposium, and won Second Place in the Best Article Competition at the 2018 IEEE International Microwave Symposium. He currently serves as the Chair for MTT TC2 and TC 21. He also serves as an Associate Editor for the IEEE TRANSACTIONS on ULTRASONICS, FERROELECTRICS, and FREQUENCY CONTROL.